PHYSICAL REVIEW B **93**, 035307 (2016)

Signature of a topological phase transition in the Josephson supercurrent through a topological insulator

M. P. Stehno,[1,*] V. Orlyanchik,[1] C. D. Nugroho,[1] P. Ghaemi,[1,2] M. Brahlek,[3,†] N. Koirala,[3] S. Oh,[3] and D. J. Van Harlingen[1,‡]
[1]*Department of Physics, University of Illinois at Urbana-Champaign, Urbana, Illinois 61801, USA*
[2]*Physics Department, City College of CUNY, New York, New York 10031, USA*
[3]*Department of Physics and Astronomy, Rutgers, The State University of New Jersey, Piscataway, New Jersey 08854, USA*

(Received 12 August 2015; revised manuscript received 17 December 2015; published 19 January 2016)

Topological insulators (TIs) hold great promise for topological quantum computation in solid-state systems. Recently, several groups reported experimental data suggesting that signatures of Majorana modes have been observed in topological insulator Josephson junctions (TIJJs). A prerequisite for the exploration of Majorana physics is to obtain a good understanding of the properties of low-energy Andreev bound states (ABSs) in a material with a topologically nontrivial band structure. Here, we present experimental data and a theoretical analysis demonstrating that the band-structure inversion close to the surface of a TI has observable consequences for supercurrent transport in TIJJs prepared on surface-doped $\mathrm{Bi_2Se_3}$ thin films. Electrostatic carrier depletion of the film surface leads to an abrupt drop in the critical current of such devices. The effect can be understood as a relocation of low-energy ABSs from a region deeper in the bulk of the material to the more strongly disordered surface, which is driven by the topology of the effective band structure in the presence of surface dopants.

DOI: 10.1103/PhysRevB.93.035307

I. INTRODUCTION

In small-gap semiconductors, strong spin-orbit interactions may cause an inversion between valence and conduction bands. This generates a new class of insulators, which are called topological insulators (TIs) due to their nontrivial band topology [1–3]. One intriguing feature of these systems is the emergence of gapless, spin-momentum-locked states (a helical metal) on the interface with ordinary insulators, i.e., regions with topologically trivial band structure, or the surfaces of the material. There has been growing interest in the properties of ordered phases of these helical states. Although, in two spatial dimensions, fluctuations prohibit spontaneous symmetry breaking [4], new phases are induced by the proximity effect when magnetic or superconducting materials are brought into contact with TIs. By coupling TIs and conventional superconductors (SCs), helical surface states with superconducting pair correlations emerge, which is of particular interest in the present context. It was argued that in-gap vortex states [5] and Andreev bound states in π-Josephson junctions between conventional superconductors that are coupled by TI surface states may be realizations of zero-energy Majorana modes [6], a fermionic mode that is its own antiparticle [7]. Early models considered an idealized scenario in which helical states existed only on a single, isolated surface of the TI, decoupled from the perfectly insulating bulk. As most of the discovered TI materials were not true insulators in the bulk, it seemed difficult to implement the concept in experiments. Later it was shown theoretically that topologically protected zero-energy modes exist also on the surface of doped, superconducting TIs up to a critical level of doping. At this doping level, a topological phase transition occurs in the superconducting TI [8–11]. Several groups demonstrated supercurrent transport in SC-TI-SC hybrid structures [12–17] as well as the ability to control the chemical potential and the magnitude of supercurrent in a TI by electrostatic gating [14,18]. Furthermore, it was argued [12,18] that the majority of the supercurrent is carried by a set of low-energy Andreev bound states located on the surface of the TI. While implicitly assumed, the role of Andreev bound states (ABSs) as boundary modes has not been studied in detail. In the following, we present critical current measurements on top-gated TIJJs for which a striking, nonmonotonous dependence on gate voltage is revealed. At the same time, the increase in normal-state resistance is gradual and featureless as carriers are depleted from the surface region of the material. Below, we will argue that this unusual behavior can be understood by recognizing that in high-quality $\mathrm{Bi_2Se_3}$ thin films, the majority of doped carriers come from Se vacancies and adsorbates on the exposed surfaces. This leads to strong band-bending, and it populates, locally, states above the band inversion point. The band crossing happens deeper in the bulk. As we will show later, the effective band mass enters the dispersion relation of low-energy ABSs in TIJJs directly, thus supercurrent transport becomes a sensitive probe of band topology in the presence of an inhomogeneous dopant distribution (disorder). We may therefore associate the observed abrupt drop in supercurrent with a topological transition in the band structure of the surface region.

II. EXPERIMENT

Recently, a new generation of high-quality bismuth-selenide TI materials became available [19]. These epitaxially grown thin films feature low levels of intrinsic doping in the bulk. The Fermi level is close to the bottom of the conduction band. Regions with higher levels of extrinsic

---

[*] Present address: MESA+ Institute for Nanotechnology and Faculty of Science, University of Twente, 7500 AE Enschede, The Netherlands; m.p.stehno@utwente.nl.

[†] Present address: Department of Materials Science and Engineering, Pennsylvania State University, University Park, PA 16802, USA.

[‡] dvh@illinois.edu

n-type doping form close to the top surface where the material becomes selenium-deficient and adsorbs impurities [20,21], and at the bottom interface due to substrate effects, as becomes apparent when the film is transferred between different types of substrates [22]. The accumulated charge leads to band-bending, which can be large enough to create a quantum-confined two-dimensional electron gas (2DEG) layer extending a few quintuple layers (QL) into the TI. In transport measurements on the as-grown films, it was found that the bulk contribution to the electrical current is negligible compared to that of the charge accumulation regions over a wide range of sample thicknesses [19]. We incorporated this material in our top-gated Josephson devices and found that we were able to deplete the charge carriers in the accumulation region significantly, thereby removing the band-bending and shifting the top-surface Dirac point up to the bulk Fermi level and beyond. This opens up an opportunity to study the interplay of band-structure effects and Andreev bound states that form in doped topological insulators.

Josephson junctions and Hall bar devices for magnetotransport measurements were fabricated side-by-side on high-quality Bi_2Se_3 thin films grown by molecular-beam epitaxy on sapphire (Al_2O_3) (0001) substrates [19,23]. The thickness of the films varied between 6 and 60 QL. To pattern the structures, we used standard electron-beam lithography techniques. The lengths of our planar Josephson junctions were set by the separation between two sputtered Nb electrodes and varied between 90 and 120 nm. The junction widths were defined by dry-etching and ranged between 0.1 and 1 μm. Top-gate electrodes were added by evaporating 70 nm of Au on top of the 40-nm-thick dielectric layer of ALD-grown alumina (Al_2O_3) or hafnia (HfO_2). After structuring, the transport properties of our Bi_2Se_3 material were characterized in magnetotransport measurements at 1.7 K and milli-Kelvin temperatures, respectively. Using the two-carrier transport model, we find excellent quantitative agreement with the results by Bansal *et al.* [19], e.g., the extracted carrier density and mobility values from a fit to the data of our 15 QL sample are $n_1 = 4 \times 10^{13}$ cm^{-2}, $\mu_1 = 700$ cm^2 V^{-1} s^{-1} and $n_2 = 4 \times 10^{12}$ cm^{-2}, $\mu_2 = 1700$ cm^2 V^{-1} s^{-1}. Similar values were obtained for all Bi_2Se_3 film thicknesses. Weak antilocalization was observed with an amplitude factor of $\alpha \simeq -\frac{1}{2}$, indicating weak antilocalization on a single surface or strong intersurface scattering [24]. The main focus of our study is the dc Josephson effect in electrostatically gated SC-TI-SC devices. The experiments were carried out in a dilution refrigerator that was placed in a shielded room. All electrical connections to the sample were heavily filtered. In the following, we present data of a junction of 0.1 μm length, 0.4 μm width, and a thickness of 15 QL, which are representative for all 15 measured samples.

III. RESULTS

The current-voltage (I-V) characteristics of a Nb-Bi_2Se_3-Nb junction are shown in Fig. 1(a) for different sample temperatures. Here, we define the critical current (I_C) of the device as the current at which a finite voltage drop develops between the two superconducting electrodes. A maximum Josephson supercurrent of $I_C^{\max} = 190$ nA was measured at temperature $T = 45$ mK. Other devices showed values of $I_C^{\max}$ between 10 and 300 nA, scaling with the width of the junction. The critical current density, $J_c \sim 3 \times 10^3$ A/cm^2, is similar to Bi_2Se_3 and Bi_2Te_3 Josephson junctions of comparable dimensions found in the literature; cf. Table I in Ref. [17]. At the lowest temperatures, the critical current becomes hysteretic [i.e., in Fig. 1(a) the retrapping current, $I_R \approx 80$ nA, is smaller than I_C for the black, red, and blue datasets]. The hysteresis characteristics are consistent with electron heating, which develops after switching the junction into the resistive state [25]. Recently, I-V hysteresis in SNS contacts under general nonequilibrium conditions was described theoretically [26]. However, the estimated intrinsic capacitance of our devices as defined in Ref. [26], $C^\star \approx 10^{-13}$ F, and the ordinary junction capacitance, $C \ll C^\star$, are too small for the effect to contribute significantly. In Fig. 1(b), a Fraunhofer-like diffraction pattern is generated by applying a small magnetic field perpendicular to the junction plane. Unusual features in the diffraction patterns of SC-TI-SC were reported in Refs. [15,27,28]. Although we observed similar characteristics in some of our devices, we did not carry out a detailed study.

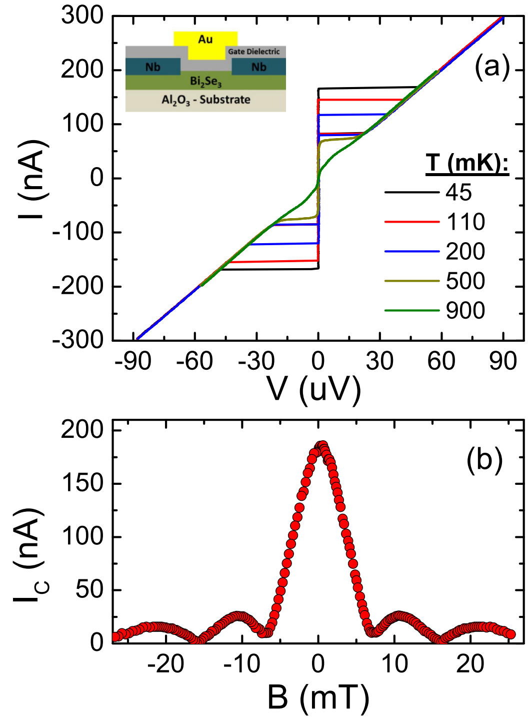

FIG. 1. Josephson junction characteristics. (a) The current-voltage characteristics of the Josephson junction at different temperatures. Inset: a schematic representation of the junction cross section. (b) The dependence of the critical current on the perpendicular magnetic field exhibits a Fraunhofer-like pattern.

Due to the formation of selenium vacancies and the accumulation of adsorbates on the exposed surfaces of the Bi_2Se_3 thin-film samples immediately after growth and during the fabrication process [20,21], our samples are electron-doped. The excess n-carriers cause downward band-bending in the charge accumulation region close to the top interface, placing the surface chemical potential firmly in the (surface-projected) bulk conduction band. By applying a negative voltage (V_G)

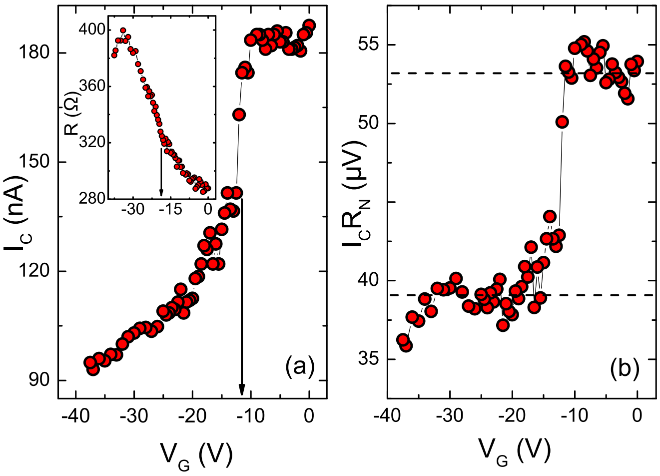

FIG. 2. Gate dependence of the Josephson critical current. (a) The critical current as a function of the gate voltage measured at $T = 50$ mK. Inset: Dependence of the normal state resistance of the junction on the gate voltage. (b) The variation of the product of the critical current and normal state resistance ($I_C R_N$) measured as a function of gate voltage. The dashed lines emphasize two values of $I_C R_N$ above and below the transition region.

to the top-gate electrode [cf. the device schematics in the inset of Fig. 1(a)], we depleted carriers from the TI surface electrostatically. In Fig. 2, we plot the critical current and the normal-state resistance of the device (inset) as a function of gate voltage. Whereas the resistance increases slowly without any prominent features down to $V_G \sim -33$ V, the critical current initially stays constant and then drops abruptly. This rapid change in I_C takes place in a narrow region of gate voltages, $\Delta V_G < 1$ V, which we call a *transition region* and mark it by its center value, the critical gate voltage $V_C \approx -12$ V. The transition region is trailed by a gradual and featureless decrease of I_C. This highly nonmonotonic behavior of $I_C(V_G)$ is reproducible. It was observed in multiple, consecutive gate voltage scans for each individual Josephson junction, and it was present in all measured devices (15 Josephson junctions). The value of V_C varied, accordingly, with the thickness and dielectric constant of the gate dielectric (Al_2O_3 or HfO_2). By contrast, the abrupt changes in I_C were never accompanied by fast variations in the normal-state resistance in any of the tested junctions. The normal state resistance of the devices, estimated by a linear fit to the I-V characteristic in a 50 μV range above the critical current, remained a smooth function of V_G and scaled with the sheet resistance of the material, which was measured in the Hall bar devices. Thus, in Fig. 2(b), the product of critical current and normal-state resistance, $I_C R_N$, which reflects the characteristic energy of the Josephson coupling, shows a distinct step at $V_G = V_C$.

IV. DISCUSSION

The prominent drop in the critical current is an usual and compelling feature. In gate-controlled 2DEG Josephson devices based on semiconductor heterostructures (*Josephson field-effect transistors* or JoFETs), the critical current is a function of carrier density, which decreases monotonously with the depletion of carriers [29]. Additional structure in the $I_C(V_G)$ appears in regimes in which the device transmission is modulated strongly, e.g., for mesoscopic conductance fluctuations in the device [30], transmission resonances [31], and conductance quantization effects [32,33]. The latter two are particularly prominent in semiconductor wire devices [34–36]. In all of the aforementioned cases, variations in the critical current concur with modulations in the device conductance, which are absent in our devices. Indeed, the relation between device conductance and applied gate field is more complicated in the case at hand. Several transport channels may coexist within a distance of the charge screening length, $\lambda_S \sim 10$ nm, from the top interface of the TI. This length scale depends on the intrinsic bulk doping of the MBE-grown Bi_2Se_3 material, which was estimated to be $n_{3D} \lesssim 5 \times 10^{17}$ cm^{-3} for the as-grown films [19]. The pristine films exhibit the same transport characteristics as our patterned devices, i.e., the two-dimensional charge-carrier density appears to be independent of the sample thickness. Thus, we conclude that the overwhelming majority of charge carriers originates from extrinsic dopants on the top and bottom interfaces while the bulk carrier density remains low. For small values of intrinsic doping and moderate surface doping, it was shown that (several) quantum-confined 2DEG bands form due to strong band-bending in the region where the surface charge is screened [19,37–39]. However, it is unlikely that the depopulation of a single 2DEG band causes a steep drop in the critical current as the number of involved Andreev bound states (ABSs) decreases $\sim k^2$ with the magnitude of the wave vector k toward the bottom of the band. Instead, we propose that the abrupt change is driven by the topology of the band itself. Below, we argue that a fraction of the supercurrent is carried by ABSs that are located on the interface between the topologically trivial region and the band-inverted section of the TI (*boundary* ABSs). The vanishing of the effective band mass at the interface allows such Andreev bands to have lower energy than in the surrounding material. As we deplete the surface charge carriers with the top-gate, we change the depth of the surface potential well and move the position where the chemical potential intersects with respect to the bottom of the band. In real space, this pushes the topological boundary from a location within the 2DEG region toward the more heavily disordered surface of the TI. As a result, the magnitude of the supercurrent drops sharply.

A. Andreev bound states on the topological boundary

To demonstrate the mechanism behind the topological transition, we present a simplified model for Andreev bound states in TIJJs based on the concepts laid out in Refs. [8–10]. Here, we assume that the majority of carriers are confined within a thin layer close to the top interface of the sample. Although the bulk and the bottom surface likely contribute to conduction, the intrinsic bulk doping is low and the electrochemical potential is close to the bottom of the bulk conduction band, where the band structure is always inverted [40]. Disregarding the exact shape of the dopant distribution for the moment, let us assume a step-function-like potential well extending a few nm—a distance comparable to the charge screening length λ_S [19,41]—into the TI material. (The case

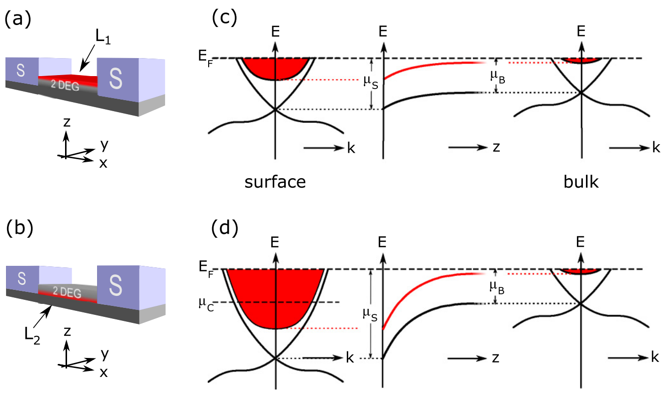

FIG. 3. Schematic of the location of low-energy Andreev bound states in a topological insulator Josephson junction. Panels (a) and (b) show the location of topological Andreev bound states for the surface chemical potentials indicated in panels (c) and (d). (The gate insulator and electrodes are omitted for clarity.) The lower part of the figure corresponds to the as-grown sample. The upper part shows the band alignment below the critical surface chemical potential. Surface and bulk chemical potentials are indicated in the left- and right-hand band diagrams, respectively. The center panels are sketches of the band-bending close to the TI surface. The shifts of the Dirac points and bulk conduction-band minima are indicated.

of band-bending and the resulting triangular potential well is discussed below.) We may then define two boundaries: L_1 is the physical interface between TI and the gate dielectric [or vacuum, see Fig. 3(a)], and L_2 is the boundary between the bulk of the TI and the surface region [see Fig. 3(b)].

Starting from the low-energy effective Hamiltonian of a doped TI with s-wave superconducting pair correlations, we model the evolution of low-energy ABSs in the surface region as carriers are added. The additional carriers lower the electrostatic potential and raise the internal chemical potential in this region. Unless stated otherwise, the term "chemical potential" will refer to the *internal* chemical potential, and the *external* chemical potential is given by the electrostatic potential. The total chemical (or *electrochemical*) potential is assumed to be constant in the $\hat{z}$ direction throughout the material. The model Hamiltonian for a doped TI reads

$$\begin{aligned} H_{\mathrm{eff}} = {} & [v_F(k_x\sigma_x + k_y\sigma_y + k_z\sigma_z)\tau_x + m(|\mathbf{k}|)\tau_z - \mu]\eta_z \\ & + \Delta[\cos(x)\eta_x + \sin(x)\eta_y]. \end{aligned} \tag{1}$$

Here, η_i are Pauli matrices that act on superconducting particle and hole states, and the representations τ_i and σ_i are chosen for orbital and (physical) spin degrees of freedom [8]. The Hamiltonian is translationally invariant along the $\hat{y}$ direction, which is in-plane and perpendicular to the current flow in the junction [see Fig. 3(a)], and k_y denotes the wave vector along $\hat{y}$. The charge-carrier concentration is determined by the chemical potential, μ, in the 2DEG region, which controls the accessible Fermi momenta, $\mathbf{k}_F$, in the band structure. These enter the equations in the form of the momentum-dependent effective-mass term for the conduction band, $m(|\mathbf{k}|)$. A simplified form of the effective-mass term, which captures the essential features of the bulk band structure of TIs, is $m(|\mathbf{k}|) = M - \epsilon|\mathbf{k}|^2$ with $M\epsilon > 0$.

At lower doping levels (i.e., closer to the Dirac point where $k = |\mathbf{k}| < M/\epsilon$), the effective mass in the surface region has the same sign as in the bulk of the TI, which is given by $m(0) = M$. The low-energy ABSs are localized at L_1, the physical surface of the TI. Further increasing the chemical potential decreases the magnitude of the effective mass $|m(k)|$, which vanishes when $k = \sqrt{M/\epsilon}$. Beyond this point, the mass term reverses its sign with respect to the bulk mass M. As derived in Appendix A, the energy difference between 2DEG ABSs and boundary ABSs at L_1 is given approximately by

$$|\Delta E| \propto \alpha \frac{m(|\mathbf{k}_F|)^2}{m(|\mathbf{k}_F|)^2 + v_F^2|\mathbf{k}_F|^2}, \tag{2}$$

where $\alpha > 0$ is of order of $|\Delta|^2/\mu$, and v_F denotes the Fermi velocity. Hence, for $m(|\mathbf{k}_f|) = 0$, the energy of 2DEG ABSs is equal to the surface bound-state energy. At this moment, the band structure in the surface region becomes topologically trivial, similar to that of an ordinary superconducting metal. In our toy model, this opens a decay channel for the boundary ABSs at L_1, and their wave function delocalizes in the entire surface region. The effect is driven purely by the band topology. As we increase the chemical potential further, we move the topological boundary to L_2, i.e., the interface between the bulk TI and the 2DEG region [see Fig. 3(b)]. Here, a different set of boundary ABSs with low energy appears after the topological transition.

B. Numerical calculations of ABSs and band-bending

The preceding analysis shows that the location of low-energy ABSs moves with the topological phase boundary. This is indeed a general feature of ABSs in doped topological superconductors, and it does not depend on a particular shape of the background potential. To illustrate the topological aspect of low-energy ABSs, and to extend our discussion to more realistic potential landscapes, we performed a series of numerical calculations that map out the shape of the ABS wave functions as we vary the background potential in the computation cell. We used a simple four-band description for strong topological insulators [8,10], and we considered s-wave superconducting pairing at the mean-field level. The band structure for our model is shown in Fig. 4(b) . For better visibility, we chose a large value for the effective pairing potential, $\Delta = 0.2$. The energies of ABSs were obtained by exact diagonalization on a lattice with 25×81 sites. We refer the reader to Appendix B for further details.

In Fig. 4, we plot the modulus of the wave-function amplitude close to the TI top surface against the chemical potential on the surface as the number of carriers is increased. For Fig. 4(a), we distributed the additional charges over the whole 2DEG region with thickness δ to create a step in the chemical potential (similar to the model in the previous section). In the "bulk" part of the lattice, $z > \delta$, the chemical potential is kept close to the bottom of the conduction band, $\mu = \mu_B = 1.7$, and in the surface region $z < \delta$, $\mu = \mu_S$ is swept through the critical value, $\mu_C \approx 1.9$. For $\mu_S < \mu_C$, the ABS wave function is localized on the surface. When the chemical potential reaches a value close to critical, the wave function abruptly delocalizes and spreads out over the

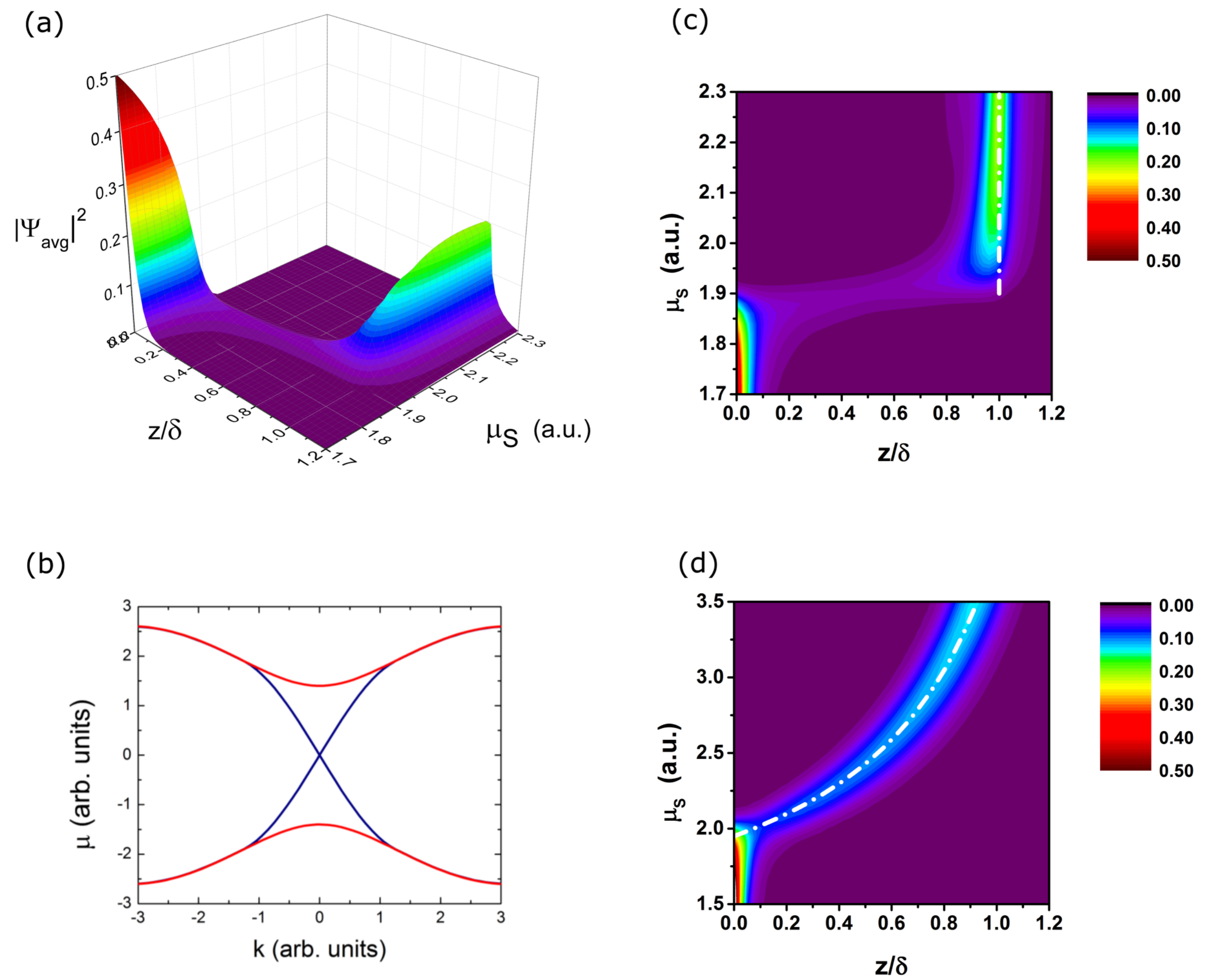

FIG. 4. Numerical calculations of the Andreev bound-state wave function (ABS WF): The in-plane averaged modulus $|\Psi_{\text{av}}|^2$ of the lowest-energy ABS WF is plotted against the surface chemical potential for a step-function potential well (a). The WF delocalizes in the entire region with critical chemical potential $\mu = 1.9$ as the surface region undergoes the topological transition (c). The band structure used in the numerical calculations is depicted in panel (b). The same calculations were carried out for a triangular potential well (d). In both calculations, the crests of the ABS WF moduli follow closely the white, dash-dotted lines, which mark the boundaries between regions of trivial (left-hand side) and inverted band structure (right-hand side) for a step-function-like (c) and a triangular potential well (d).

whole 2DEG region. Further increasing the chemical potential, $\mu_S > \mu_C$, pins the wave function to the boundary between the 2DEG region and the bulk part of the lattice [marked by a white, dash-dotted line in Fig. 4(c)].

The effect is not limited to step-function-like potential wells. For Fig. 4(d), we assumed a triangular potential well and scaled well width and depth to resemble the band-bending in our samples ($\delta \sim \lambda_S$). Again, we fixed the chemical potential in the lower part of the lattice below μ_C and varied the surface chemical potential μ_S between 1.5 and 3.5 (for detailed estimates of band-bending in our samples, see the next paragraph). Again, we observe that the ABS wave function, which attaches to the surface for smaller values of μ_S, shifts away from it when μ_S surpasses μ_C. The width of the transition region is comparable to the pairing potential, $|\mu - \mu_C| \simeq \Delta$. Past the critical point, the crest of the wave function moves with the topological boundary, visualized by the white, dash-dotted line in Fig. 4(d) .

A central supposition in our discussion is that surface band-bending is strong enough to populate states with large k vectors. Using the parameters of Ref. [40], we estimate that the band-structure topology changes ∼233 meV above the bottom of the conduction band. To estimate the band-bending for the sample presented here, we solved the Poisson equation for a 15 QL film of Bi_2Se_3 with moderate bulk doping numerically. We chose to use material parameters obtained by Jenkins *et al.* [42,43], who studied films grown by the Rutgers group under identical conditions to those of our films. Here, the bulk carriers are assumed to be n-type with a density $n_b = 4.3 \times 10^{17}/\text{cm}^{-3}$ and an effective mass $m = 0.19 m_e$ [43]. Similar values have been reported in Refs. [20,21]. The majority of carriers are doped on the surface or confined within a few quintuple layers of it, which is approximated by a surface sheet carrier density equal to the carrier density of the majority band in our two-band model fit, $n_S = n_1 = 4 \times 10^{13}\ \text{cm}^{-2}$. Using electrostatic boundary conditions with dielectric constants $\epsilon_r^G = 10$ and

$\epsilon_r^{\mathrm{TI}} = 100$ for gate dielectric (Al_2O_3) and Bi_2Se_3, respectively, we obtained the carrier distribution and the downward shift of the bands close to the surface as a function of the applied gate voltage, V_G. We found that band-bending (of the conduction band) exceeds 350 meV at $V_G = 0$ V, which validates the assumptions we made earlier. On the film surface, the Fermi level crosses the band inversion point at $V_G = -11.85$ V, which is in good agreement with the measured critical gate voltage value, $V_C \sim -12$ V, despite the coarse approximations in our modeling. Here, we would like to point out that all TIJJs prepared on the same TI film have similar critical voltage values, whereas a larger variation is observed between devices of different films. Further, the critical voltage scales with thickness and the dielectric constant of the gate dielectric, as expected.

C. Supercurrent suppression and normal-state resistance

The total supercurrent for a given phase difference ϕ across the junction is obtained by summing the phase gradient of the ABS energy with a thermal weighting factor over all Andreev bound states,

$$I_C \propto -\sum_{E_n \geqslant 0} \frac{\partial E_n}{\partial \phi} \tanh\left(\frac{E_n}{2k_B T}\right), \tag{3}$$

where E_n is the energy of the nth ABS, k_B is the Boltzmann constant, and T is the temperature. For fully transparent SC-TI interfaces, the energies of the ABS modulate strongly with ϕ, and the lowest Andreev bands cross at zero energy for $\phi = \pi$, i.e., a Majorana zero-mode forms; cf. the explicit calculations of $E_n(\phi)$ in Refs. [44,45]. The amplitude of the ABS wave function decreases with increasing wave-vector mismatch between SC and TI [45]. The degeneracy at zero energy is lifted when (tunnel) barriers are introduced at the SC-TI interfaces [46]. Both effects diminish the supercurrent that is carried by individual ABSs. In the case of strong band-bending, however, we have many ABSs in the TIJJ. We access a region of k space where wave-vector mismatch and barrier strength evolve monotonically as we deplete the 2DEG region. Consequently, it is unlikely that a small variation in gate voltage would cause a dramatic change in barrier transmission that could explain the observed abrupt drop in critical current.

In a topological insulator, the effective mass gaps the ABS spectrum. This leads to unusual behavior in the presence of band-bending on the surface of our TIJJs. Unlike the bound-state wave functions in a triangular potential well, the Andreev bound states of the lowest-energy band are strongly localized on the boundary between regions with different band topology where the effective mass vanishes. These modes carry the most supercurrent per mode [cf. Eq. (3)]. The topological boundary moves toward the surface of the TI as we deplete carriers in the device. An overlap with the highly disordered TI surface develops only when the surface chemical potential reaches the critical value μ_C, and the wave function is pinned on the surface below μ_C. Therefore, the pronounced drop in critical current reflects a difference in transmission probability for phase-coherent transport between the disordered surface and the region with lower defect density below. The observed step in the $I_C R_N$ product [see Fig. 2(b)] indicates a qualitative change in the proximity coupling.

Unlike other scenarios, the topological transition model allows us to understand why the normal resistance remains a smooth function of the applied gate voltage in our TIJJ devices. Whereas a sudden change in the tunneling probability at the interface barriers, or e.g., the pinching-off of several conduction channels, would affect normal-state resistance and supercurrent equally, the unusual effect arises when superconducting pairing is introduced in the presence of band inversion. It is intimately connected with the notion of low-energy ABSs as boundary modes of a superconducting TI, and it can only be detected when the dispersion relation of Andreev bound states $E(\phi)$ is nonsinusoidal and has a low-energy band. Here, we would like to point to recently published work that indicates the presence of low-energy ABSs in TIJJs. In that work Kurter *et al.* [27,28] reported anomalies in the diffraction patterns of Josephson junctions and superconducting quantum-interference devices (SQUIDs) made from exfoliated Bi_2Se_3 and they explained these by a nonsinusoidal contribution to the current-phase relationship (CPR) of TIJJs. The nonsinusoidal component is attributed to the presence of low-energy ABSs in the junctions. The authors also observed a step in the critical current versus gate voltage dependence, which shows that the effect is not related to a specific TI material or fabrication method.

V. CONCLUSION

In conclusion, we presented experimental evidence for a topological phase transition in the bulk band of a doped, proximity-coupled three-dimensional topological insulator. The hallmark of the transition is a shift in the spatial location of low-energy Andreev bound states that follow the position of the topological boundary. In particular, we demonstrated that the charge-accumulation zone (2DEG channel) close to the surface of a doped 3D TI can be driven through the transition by electrostatically depleting surface carriers with a top-gate. This is registered as a jump in the magnitude of the critical current of the Josephson junctions. The abrupt change occurs when the chemical potential of the surface 2DEG region lies within the (surface-projected) bulk band and correlates with a sign change of the effective mass in the TI band-structure model. The transition in the band structure topology of the gapped, 2DEG proximity region results in an altered supercurrent flow pattern due to a displacement of low-energy ABSs toward the disordered device surface. Consequently, the change in the effective Josephson coupling leads to a sudden and unusual drop in the $I_C R_N$ product. Importantly, we do not make the assumption that the bulk of the topological insulator is insulating. The mechanism also works when the bulk is conducting, but the bulk Fermi level must be below the critical chemical potential for which the topological phase transition occurs. Our results also indicate that a sizable fraction of supercurrent is carried by low-energy Andreev bound states located on the boundary between topologically trivial and band-inverted regions of the topological insulator (boundary ABSs), but not necessarily on the surface of the topological insulator, as is frequently implied (e.g., see Refs. [12,18]). Exploration of Majorana physics in three-dimensional topological insulators requires control over the spatial location of zero-energy Andreev states. Our study is directed toward discovering an effective way of manipulating low-energy Andreev bound states in 3D TI Josephson devices.

ACKNOWLEDGMENTS

We would like to thank Ashvin Vishwanath, Taylor Hughes, Jeffrey Teo, Eduardo Fradkin, and Alexander Brinkman for useful discussions. V.O., M.P.S., C.D.N., and D.J.V.H. acknowledge funding by Microsoft Station-Q. For the device fabrication, we acknowledge use of the facilities of the Frederick Seitz Materials Research Laboratory at the University of Illinois at Urbana-Champaign. P.G. acknowledges support from NSF DMR-1064319. M.B., N.K, and S.O. are supported by ONR (N000141210456) and Gordon and Betty Moore Foundation's EPiQS Initiative (GBMF4418).

APPENDIX A: LOW-ENERGY ANDREEV STATES IN THE BULK AND ON THE SURFACE OF DOPED TOPOLOGICAL INSULATORS

Gapless helical surface states are considered to be the characteristic feature of topological insulators. Topological properties of bulk bands are difficult to observe. However, close to a transition, the Andreev-bound-state spectrum in Josephson junctions depends sensitively on the bulk-band topology, which allows us to detect a clear signature of a topological transition in the band.

At wave vectors close to different time-reversal symmetric points (TRs), the Hamiltonian of bulk TI bands resembles the three-dimensional massive Dirac Hamiltonian. At the TRs, a relative change in the sign of the mass term in the Dirac Hamiltonian occurs [47]. As a result, the minimal effective Hamiltonian for the wave vectors near the bottom of the conduction band of 3D TIs is given by

$$\mathcal{H} = v_F \tau_x \, \boldsymbol{\sigma} \cdot \mathbf{k} + \tau_z \, m(\mathbf{k}), \tag{A1}$$

where $\boldsymbol{\sigma} = (\sigma_x, \sigma_y, \sigma_z)$ are the Pauli matrices acting on spin space; τ_x, τ_y are the Pauli matrices acting on orbital space; and $\mathbf{k}$ is the wave vector relative to the TR at the bottom of the conduction band. The momentum-dependent mass term $m(\mathbf{k}) = M - \epsilon|\mathbf{k}|^2$, with $M\epsilon > 0$, changes sign at $|\mathbf{k}| = \sqrt{M/\epsilon}$. It was shown before that the topological properties of the superconducting phase of a doped topological insulator change when the chemical potential corresponds to the wave vectors at which the effective mass $m(\mathbf{k})$ vanishes [8–10]. One manifestation of this topological transition is the appearance of edge modes, e.g., the zero-energy Majorana states at the ends of a vortex passing through a doped topological insulator [6,8–10]. In this case, the bound states that extend along the vortex [5,8–10] become gapless at the transition and provide a channel for coupling Majorana modes at both ends of the vortex, thus allowing them to annihilate. Indeed, zero modes in the energy spectrum of the superconducting bulk were the first theoretical evidence for a topological phase transition as a function of the doping level in doped TIs [8]. Later the result was confirmed by looking directly at the evolution of Majorana states at the end of the vortex as a function of the chemical potential [10,48].

An analogous scenario is realized in a topological insulator Josephson junction (TIJJ). When the chemical potential is in the bulk gap of the TI, ABSs are found only on the TI surface. At a phase difference of π, two of the localized Andreev states in a TIJJ are zero-energy Majorana modes [6]. On the other hand, when the TI is doped and the chemical potential enters the conduction band, superconductivity is induced in the bulk, and additional ABSs are formed throughout the TIJJ. Similar to the topological transition in the vortex, the energy of ABSs evolves with the chemical potential in the TI. As we move it through the bulk band of the TI, the shape of the Fermi surface changes, i.e., the Fermi surface is composed of different sets of $\mathbf{k}$ states. For particular $\mathbf{k}$ vectors, the mass term $m(\mathbf{k})$ vanishes, and the band structure undergoes a topological phase transition. An important signature is that the ABS spectrum becomes gapless, thus decay channels for Majorana modes open, which—at this point—can no longer exist on the surface.

The presence of Majorana modes on the surface and of gapless modes in the bulk of TIJJs corresponds precisely to a phase difference of π. Under simplifying assumptions, it can be shown that this condition is fulfilled in TIJJs at maximum critical current [44]. We are interested, however, in the full evolution of low-energy Andreev states. Thus, we study the general case of TIJJs with an arbitrary phase difference. In what follows, we first derive the energy of ABSs on the surface of a narrow junction. Next, we find the energy of bulk ABSs and show that it decreases as the magnitude of the effective mass, $|m(\mathbf{k})|$, decreases. In particular, we see that—for vanishing effective mass $m(\mathbf{k})$—the (finite) energy of the lowest-lying ABS on the surface will become equal to the energy of the bulk Andreev states even if the phase of the junction is not π.

When the chemical potential is in the bulk band gap of the TI, the only gapless states are helical states localized on the boundary of the TI sample. They realize the gapless, two-dimensional Dirac Hamiltonian:

$$\mathcal{H}_s = i v_F \boldsymbol{\sigma} \cdot \mathbf{k}, \tag{A2}$$

where $\boldsymbol{\sigma} = (\sigma_x, \sigma_y)$ are the Pauli matrices in the bases $(\psi_\uparrow, \psi_\downarrow)$, and ψ_σ is the electronic state with spin σ localized on the surface of the TI.

The low-energy effective Hamiltonian describing a Josephson junction on the surface of the TI with supercurrent along $\hat{x}$ (such that the superconducting ϕ varies in the $\hat{x}$ direction) is given by [8]

$$H = (-i v_F \nabla \cdot \boldsymbol{\sigma} - \mu)\eta_z + \Delta\{\cos[\phi(x)]\eta_x + \sin[\phi(x)]\eta_y\}, \tag{A3}$$

with a convenient choice of bases $(\psi_\uparrow, \psi_\downarrow, \psi_\downarrow^\dagger, -\psi_\uparrow^\dagger)^T$. In this Hamiltonian, the Fermi velocity at chemical potential μ is denoted by v_F, and Δ is the superconducting gap. The matrices $\boldsymbol{\sigma}$ act on physical spin space (which is locked with the momentum), whereas the η_i act on the superconducting particle-hole space.

As the Hamiltonian, Eq. (A3), is invariant under translation along $\hat{y}$, the momentum k_y in this direction is conserved. The lowest-energy Andreev states in the junction correspond to

$k_y = 0$, for which Eq. (A3) reduces to

$$[(-iv_F\partial_x\sigma_x - \mu)\eta_z + \Delta\{\cos[\phi(x)]\eta_x + \sin[\phi(x)]\eta_y\}]|v\rangle = E|v\rangle. \tag{A4}$$

As an operator, σ_x commutes with the above Hamiltonian. Therefore, it is possible to divide the eigenstates into two separate sets with eigenvalue $\langle\sigma_x\rangle = 1$ or -1:

$$[(\mp iv_F\partial_x - \mu)\eta_z + \Delta\{\cos[\phi(x)]\eta_x + \sin[\phi(x)]\eta_y\}]|v\rangle = E|v\rangle, \tag{A5}$$

where the negative (positive) sign of the first term corresponds to $\langle\sigma_x\rangle = 1$ (or -1), respectively. Similarly, at finite positive chemical potential ($\mu > 0$), the right and left Fermi points correspond to states with opposite σ_x eigenvalues—$\langle\sigma_x\rangle > 0$ for the right and $\langle\sigma_x\rangle < 0$ for the left Fermi point, respectively.

The eigenvectors $|v\rangle$ have the form $|v\rangle = e^{ik_\pm x}|u\rangle$, where $k_\pm = \pm k_F = \pm\frac{\mu}{v_F}$ are the Fermi momenta at the two Fermi points, and the eigenvectors $|u\rangle$ satisfy

$$[(\mp iv_F\partial_x)\eta_z + \Delta\{\cos[\phi(x)]\eta_x + \sin[\phi(x)]\eta_y\}]|u\rangle = E|u\rangle. \tag{A6}$$

A short Josephson junction is modeled by the following phase distribution:

$$\begin{aligned} \phi(x) &= 0 \quad \text{for } x < 0, \\ \phi(x) &= \phi_0 \quad \text{for } x \geqslant 0. \end{aligned} \tag{A7}$$

Since we are interested in in-gap Andreev states, we define $E = \Delta\cos(\beta)$ with $0 \leqslant \beta \leqslant \pi$. The eigenvector $|u\rangle$ has the form

$$|u\rangle = e^{\frac{\kappa\Delta}{v_F}x}\begin{pmatrix} a \\ b \end{pmatrix}, \tag{A8}$$

where the vectors $(a,b)^T$ satisfy the following equation:

$$\Delta\begin{pmatrix} \mp i\kappa - \cos(\beta) & e^{i\phi(x)} \\ e^{-i\phi(x)} & \pm i\kappa - \cos(\beta) \end{pmatrix}\begin{pmatrix} a \\ b \end{pmatrix} = 0, \tag{A9}$$

which leads to $\kappa = \sin(\beta)$ for $x < 0$ and $\kappa = -\sin(\beta)$ for $x > 0$. Notice, since we have $0 \leqslant \beta \leqslant \pi$, it follows that $\sin(\beta) \geqslant 0$. The wave functions are

$$x < 0: \begin{pmatrix} a \\ b \end{pmatrix} = \frac{1}{\sqrt{2}}\begin{pmatrix} 1 \\ e^{\pm i\beta} \end{pmatrix}, \tag{A10}$$

$$x \geqslant 0: \begin{pmatrix} a \\ b \end{pmatrix} = \frac{1}{\sqrt{2}}\begin{pmatrix} 1 \\ e^{i(\phi\mp\beta)} \end{pmatrix}. \tag{A11}$$

From the continuity condition at $x = 0$, we obtain $\beta = \frac{\phi}{2}$ for the right Fermi point and $\beta = \pi - \frac{\phi}{2}$ for the left Fermi point such that $0 \leqslant \phi,\ \beta \leqslant \pi$. Close to the right and left Fermi points, the energies of the ABSs are found to be $E = \Delta\cos(\phi/2)$ and $E = \Delta\cos(\pi - \phi/2) = -\Delta\cos(\phi/2)$, respectively. The two modes correspond to eigenvalues of σ_x with opposite sign, thus there is no mixing between them. Importantly, their wave functions stay localized on the surface of the TI because bulk ABSs have larger energy. In what follows, we show that the energy of Andreev states in the bulk of a TIJJ is always larger than the energy of low-energy Andreev states on the surface, unless the chemical potential corresponds to the Fermi wave vectors $\mathbf{k}_F$ where the effective mass $|m(\mathbf{k}_F)|$ vanishes.

The low-energy Hamiltonian in the bulk of a topological insulator is the massive Dirac Hamiltonian, Eq. (A1). Adding terms for superconducting pairing and the finite chemical potential, the Hamiltonian reads

$$\begin{aligned} H_b = {} & [v_F(\boldsymbol{\nabla}\cdot\boldsymbol{\sigma})\tau_x + m(|\mathbf{k}|)\tau_z - \mu]\eta_z \\ & + \Delta\{\cos[\phi(x)]\eta_x + \sin[\phi(x)]\eta_y\}. \end{aligned} \tag{A12}$$

Here, we would like to point out that the minimal model for TI bulk states has two orbitals, and another set of Pauli matrices, τ_i, for orbital space had to be introduced in the Hamiltonian. Therefore, the algebraic structure of the wave function is different for bulk and surface states.

Similar to surface states, low-energy bulk ABSs have momenta parallel to the $\hat{x}$ direction (i.e., $k_y = k_z = 0$), and the effective Hamiltonian is

$$\begin{aligned} H_b = {} & [v_F k_x\sigma_x\tau_x + m(|\mathbf{k}|)\tau_z - \mu]\eta_z \\ & + \Delta\{\cos[\phi(x)]\eta_x + \sin[\phi(x)]\eta_y\}. \end{aligned} \tag{A13}$$

Again, the operator σ_x commutes with the effective Hamiltonian, thus we can divide the eigenstates into two separate sets with eigenvalue $\langle\sigma_x\rangle = 1$ or -1:

$$\begin{aligned} H_b = {} & [\pm v_F k_x\tau_x + m(|\mathbf{k}|)\tau_z - \mu]\eta_z \\ & + \Delta\{\cos[\phi(x)]\eta_x + \sin[\phi(x)]\eta_y\}. \end{aligned} \tag{A14}$$

In the following, we only present the solution for $\langle\sigma_x\rangle = 1$, which corresponds to the $+$ sign for the first term of H_b. The case of $\langle\sigma_x\rangle = -1$ can be treated identically. When the chemical potential is in the conduction band, the spectrum and orbital wave function are solutions of the kinetic Hamiltonian, $\mathcal{H} = v_F\tau_x k_x + \tau_z m(\mathbf{k})$. Its eigenvalues and eigenfunctions are given by

$$\begin{aligned} \mathcal{E}(k_x) &= \sqrt{v_F^2k_x^2 + m(|k_x|)^2}, \\ |\Phi_\tau(k_x)\rangle &= \frac{1}{\mathcal{N}}\left(m(|k_x|), \sqrt{m(|k_x|)^2 + v_F^2k_x^2} - v_Fk_x\right)^T, \end{aligned} \tag{A15}$$

with the normalization factor $\mathcal{N}^2 = 2m(|k_x|)^2 + 2v_F^2k_x^2 - 2v_Fk_x\sqrt{m(|k_x|)^2 + v_F^2k_x^2}$. The low-energy ABSs close to the Fermi points, $k_F^\pm = \pm\frac{\sqrt{\mu^2 - m(|k_F|)^2}}{v_F}$, are derived by setting $k_x = k_F^\pm \mp i\partial_x$ in Eq. (A14) and by projecting onto the corresponding orbital wave functions $|\Phi_\tau(k_F^\pm)\rangle$. We obtain the equations

$$[(\mp iv_F\partial_x)\eta_z + \Delta\{\cos[\phi(x)]\eta_x + \sin[\phi(x)]\eta_y\}]|w\rangle = E|w\rangle. \tag{A16}$$

The Hamiltonian in Eq. (A16) is formally identical to the previously discussed Hamiltonian, Eq. (A6). For the energies at the right and left Fermi points, we have $E = \Delta\cos(\phi/2)$ and $E = \Delta\cos(\pi - \phi/2) = -\Delta\cos(\phi/2)$. Unlike before, the wave functions at the two Fermi points correspond to the same eigenvector of σ_x, and the orbital parts of the wave functions, Eq. (A15), are—in general—not orthogonal. Since the phase ϕ varies along the $\hat{x}$ direction, states at the two Fermi points are scattered into each other and repel.

The energy shift due to scattering is calculated using second-order perturbation theory. It is proportional to the orbital overlap of the wave functions at the two Fermi points, i.e., $\langle \Phi_\tau(k_f^-)|\Phi_\tau(k_f^+)\rangle = \frac{|m(|k_F|)|}{\sqrt{m(|k_F|)^2+v_F^2k_F^2}}$, and it takes the form

$$E = \pm\left(\Delta|\cos(\phi/2)| + \alpha\frac{m(|k_F|)^2}{m(|k_F|)^2+v_F^2k_F^2}\right), \tag{A17}$$

where $\alpha > 0$. Assuming the magnitude of the superconducting gap is equal on the surface and in the bulk, it follows that the energies of bulk Andreev states are larger than those of surface Andreev states unless $m(\mathbf{k}_F) = 0$.

APPENDIX B: FURTHER DETAILS ABOUT THE NUMERICAL CALCULATIONS

We studied the structure of low-energy Andreev states in TIJJs for different background potentials numerically. A simple discrete model for TIs includes four orbitals on a cubic lattice with orbital-dependent nearest-neighbor hopping [8,49]. We implement superconductivity at the mean-field level, i.e., we double the number of orbitals at each lattice site to represent superconducting particle and hole states, and we add a coupling term between the two sectors. Allowing the phase of this coupling to vary along the $\hat{x}$ direction, we can model a TIJJ.

As we set the momentum along the $\hat{y}$ direction (i.e., "parallel" to the junction) equal to zero, it is sufficient to discretize the Hamiltonian on a square, real-space lattice with dimensions $L_x \times L_z$, for which the two site labels (x,z) are chosen along the directions of the superconducting phase variation, $\hat{x}$, and the chemical potential shift, $\hat{z}$. In the simplest case, band-bending on the surface of the TI is modeled by varying the chemical potential for sites with index $0 < z < \delta = L_z/2$ while keeping it fixed close to the bottom of the conduction band for sites with $z > \delta$. We then solve the discrete Hamiltonian exactly and plot the (in-plane averaged) wave-function amplitudes associated with the lowest-energy ABSs against the chemical potential in the surface layer; see Fig. 4(a). We observe that, as the chemical potential enters the conduction band in our model, $\mu \sim 1.7$, most of the weight of the ABS wave functions remains close to the boundary of the model (i.e., at $L_z = 0$). When we further increase the chemical potential, the wave function spreads gradually across the surface region. As the critical chemical potential ($\mu_C \approx 1.9$) is reached and the effective mass vanishes [$m(\mathbf{k}_F) = 0$], the wave function is fully delocalized and extends throughout the region (i.e., all sites where $0 < z < \delta$). Past the critical value μ_C, the ABSs are strongly localized at $z = L_z/2$, which is the interface between the—now—topologically trivial surface and the band-inverted bulk. We would like to point out that the wave function has another maximum on the bottom surface ($z = L_z$), which we cut off in Figs. 4(a) and 4(c) for clarity.

In Fig. 4(d), we show the ABS wave function for a triangular potential, parametrized by the chemical potential on the surface of the TI, μ_S. Again, we fixed the chemical potential in the bottom part of the lattice, $z > \delta = 0.75L_z$, below μ_C and varied the chemical potential across the upper part linearly. Only the wave function in the upper part of the lattice is shown. For surface potentials below μ_C, the wave function is pinned on the surface of the TI. Above the critical potential, the ABSs of the lowest energy band are strongly localized on the topological phase boundary, which is indicated by the white, dash-dotted line in Fig. 4(d). The ABS wave function spreads over a region with chemical potential close to critical, $|\mu - \mu_C| \sim \Delta$, but it has no overlap with the TI surface. Only when the surface chemical potential reaches the critical value do low-energy ABSs merge with the surface, and they become fully localized there when $\mu_S < \mu_C$.

This clearly demonstrates that in a doped topological insulator, where superconductivity is induced in the bulk (in addition to the surface states), the energies of low-energy bulk Andreev bound states are related to the magnitude of the effective mass of the bulk band and have a minimum when the effective mass vanishes. At this point, the energies of boundary and bulk ABSs are equal, which couples them and annihilates the boundary modes. Most prominently, this mechanism destroys surface Majorana modes when the bulk substrate undergoes a topological transition, which makes it relevant in a wider context. Experimental signatures of the spatial displacement of boundary ABSs due to a topological transition in the bulk band are discussed in the main text.

---

[1] J. Moore, Nat. Phys. **5**, 378 (2009).

[2] M. Z. Hasan and C. L. Kane, Rev. Mod. Phys. **82**, 3045 (2010).

[3] X.-L. Qi and S.-C. Zhang, Rev. Mod. Phys. **83**, 1057 (2011).

[4] N. D. Mermin and H. Wagner, Phys. Rev. Lett. **17**, 1133 (1966).

[5] C. Caroli, P. De Gennes, and J. Matricon, Phys. Lett. **9**, 307 (1964).

[6] L. Fu and C. L. Kane, Phys. Rev. Lett. **100**, 096407 (2008).

[7] F. Wilczek, Nat. Phys. **5**, 614 (2009).

[8] P. Hosur, P. Ghaemi, R. S. K. Mong, and A. Vishwanath, Phys. Rev. Lett. **107**, 097001 (2011).

[9] C.-K. Chiu, P. Ghaemi, and T. L. Hughes, Phys. Rev. Lett. **109**, 237009 (2012).

[10] H.-H. Hung, P. Ghaemi, T. L. Hughes, and M. J. Gilbert, Phys. Rev. B **87**, 035401 (2013).

[11] P. Ghaemi and V. P. Nair, arXiv:1506.05103 [Phys. Rev. Lett. (to be published)].

[12] M. Veldhorst, M. Snelder, M. Hoek, T. Gang, V. K. Guduru, X. L. Wang, U. Zeitler, W. G. van der Wiel, A. A. Golubov, H. Hilgenkamp, and A. Brinkman, Nat. Mater. **11**, 417 (2012).

[13] D. Zhang, J. Wang, A. M. DaSilva, J. S. Lee, H. R. Gutierrez, M. H. W. Chan, J. Jain, and N. Samarth, Phys. Rev. B **84**, 165120 (2011).

[14] B. Sacépé, J. B. Oostinga, J. Li, A. Ubaldini, N. J. G. Couto, E. Giannini, and A. F. Morpurgo, Nat. Commun. **2**, 575 (2011).

[15] J. R. Williams, A. J. Bestwick, P. Gallagher, S. S. Hong, Y. Cui, A. S. Bleich, J. G. Analytis, I. R. Fisher, and D. Goldhaber-Gordon, Phys. Rev. Lett. **109**, 056803 (2012).

[16] L. Galletti, S. Charpentier, P. Lucignano, D. Massarotti, R. Arpaia, F. Tafuri, T. Bauch, Y. Suzuki, A. Tagliacozzo, K. Kadowaki, and F. Lombardi, J. Phys. C **503**, 162 (2014).

[17] L. Galletti, S. Charpentier, M. Iavarone, P. Lucignano, D. Massarotti, R. Arpaia, Y. Suzuki, K. Kadowaki, T. Bauch, A. Tagliacozzo, F. Tafuri, and F. Lombardi, Phys. Rev. B **89**, 134512 (2014).

[18] S. Cho, B. Dellabetta, A. Yang, J. Schneeloch, Z. Xu, T. Valla, G. Gu, M. J. Gilbert, and N. Mason, Nat. Commun. **4**, 1689 (2013).

[19] N. Bansal, Y. S. Kim, M. Brahlek, E. Edrey, and S. Oh, Phys. Rev. Lett. **109**, 116804 (2012).

[20] M. Brahlek, Y. S. Kim, N. Bansal, E. Edrey, and S. Oh, Appl. Phys. Lett. **99**, 012109 (2011).

[21] R. Valdes Aguilar, L. Wu, A. V. Stier, L. S. Bilbro, M. Brahlek, N. Bansal, S. Oh, and N. P. Armitage, J. Appl. Phys. **113**, 153702 (2013).

[22] N. Bansal, M. R. Cho, M. Brahlek, N. Koirala, Y. Horibe, J. Chen, W. Wu, Y. D. Park, and S. Oh, Nano Lett. **14**, 1343 (2014).

[23] N. Bansal, Y. S. Kim, E. Edrey, M. Brahlek, Y. Horibe, K. Iida, M. Tanimura, G.-H. Li, T. Feng, H.-D. Lee, T. Gustafsson, E. Andrei, and S. Oh, Thin Solid Films **520**, 224 (2011).

[24] D. Kim, P. Syers, N. P. Butch, J. Paglione, and M. S. Fuhrer, Nat. Commun. **4**, 2040 (2013).

[25] H. Courtois, M. Meschke, J. T. Peltonen, and J. P. Pekola, Phys. Rev. Lett. **101**, 067002 (2008).

[26] D. S. Antonenko and M. A. Skvortsov, Phys. Rev. B **92**, 214513 (2015).

[27] C. Kurter, A. D. K. Finck, P. Ghaemi, Y. S. Hor, and D. J. Van Harlingen, Phys. Rev. B **90**, 014501 (2014).

[28] C. Kurter, A. D. K. Finck, Y. S. Hor, and D. J. Van Harlingen, Nat. Commun. **6**, 7130 (2015).

[29] T. Schäpers, *Superconductor/Semiconductor Junctions*, Springer Tracts in Modern Physics Vol. 174 (Springer, Berlin, 2001).

[30] H. Takayanagi, J. B. Hansen, and J. Nitta, Phys. Rev. Lett. **74**, 166 (1995).

[31] H. Takayanagi and T. Akazaki, Jpn. J. Appl. Phys. **34**, 4552 (1995).

[32] H. Takayanagi, T. Akazaki, and J. Nitta, Phys. Rev. Lett. **75**, 3533 (1995).

[33] T. Bauch, E. Hürfeld, V. M. Krasnov, P. Delsing, H. Takayanagi, and T. Akazaki, Phys. Rev. B **71**, 174502 (2005).

[34] Y.-J. Doh, J. A. v. Dam, A. L. Roest, E. P. A. M. Bakkers, L. P. Kouwenhoven, and S. D. Franceschi, Science **309**, 272 (2005).

[35] J. Xiang, A. Vidan, M. Tinkham, R. M. Westervelt, and C. M. Lieber, Nat. Nanotech. **1**, 208 (2006).

[36] S. Abay, D. Persson, H. Nilsson, H. Q. Xu, M. Fogelstrm, V. Shumeiko, and P. Delsing, Nano Lett. **13**, 3614 (2013).

[37] M. Bianchi, D. Guan, S. Bao, J. Mi, B. B. Iversen, P. D. King, and P. Hofmann, Nat. Commun. **1**, 128 (2010).

[38] D. Galanakis and T. D. Stanescu, Phys. Rev. B **86**, 195311 (2012).

[39] M. Brahlek, N. Koirala, N. Bansal, and S. Oh, Solid State Commun. **215-216**, 54 (2015).

[40] H. Zhang, C.-X. Liu, X.-L. Qi, X. Dai, Z. Fang, and S.-C. Zhang, Nat. Phys. **5**, 438 (2009).

[41] H. Steinberg, J.-B. Laloe, V. Fatemi, J. S. Moodera, and P. Jarillo-Herrero, Phys. Rev. B **84**, 233101 (2011).

[42] G. S. Jenkins, A. B. Sushkov, D. C. Schmadel, M.-H. Kim, M. Brahlek, N. Bansal, S. Oh, and H. D. Drew, Phys. Rev. B **86**, 235133 (2012).

[43] G. S. Jenkins, D. C. Schmadel, A. B. Sushkov, H. D. Drew, M. Bichler, G. Koblmueller, M. Brahlek, N. Bansal, and S. Oh, Phys. Rev. B **87**, 155126 (2013).

[44] C. T. Olund and E. Zhao, Phys. Rev. B **86**, 214515 (2012).

[45] M. Snelder, M. Veldhorst, A. A. Golubov, and A. Brinkman, Phys. Rev. B **87**, 104507 (2013).

[46] A. Furusaki and M. Tsukada, Phys. Rev. B **43**, 10164 (1991).

[47] L. Fu and C. L. Kane, Phys. Rev. B **76**, 045302 (2007).

[48] C.-K. Chiu, M. J. Gilbert, and T. L. Hughes, Phys. Rev. B **84**, 144507 (2011).

[49] P. Hosur, S. Ryu, and A. Vishwanath, Phys. Rev. B **81**, 045120 (2010).